ELSEVIER

Physica D 163 (2002) 166–183

PHYSICA D

www.elsevier.com/locate/physd

Mean flow in hexagonal convection: stability and nonlinear dynamics

Yuan-Nan Young*, Hermann Riecke

Department of Engineering Sciences and Applied Mathematics, Northwestern University, 2145 Sheridan Rd., Evanston, IL 60208, USA

Received 26 July 2001; received in revised form 23 November 2001; accepted 11 December 2001
Communicated by F.H. Busse

Abstract

Weakly nonlinear hexagon convection patterns coupled to mean flow are investigated within the framework of coupled Ginzburg–Landau equations. The equations are in particular relevant for non-Boussinesq Rayleigh–Bénard convection at low Prandtl numbers. The mean flow is found to: (1) affect only one of the two long-wave phase modes of the hexagons, and (2) suppress the mixing between the two phase modes. As a consequence, for small Prandtl numbers the transverse and the longitudinal phase instability are expected to occur in sufficiently distinct parameter regimes that they can be studied separately. Through the formation of penta–hepta defects, they lead to different types of transient disordered states. The results for the dynamics of the penta–hepta defects shed light on the persistence of grain boundaries in such disordered states.

Keywords: Hexagon pattern; Mean flow; Ginzburg–Landau equation; Nonlinear phase equation; Stability analysis; Penta–hepta defect; Grain boundary

1. Introduction

Roll patterns in Rayleigh–Bénard convection of a fluid layer heated from below have been explored extensively over the years as a paradigmatic system to study the succession of transitions from ordered to disordered and eventually turbulent states (for a recent review, see [1]). For small convection amplitudes a weakly nonlinear description in terms of a Newell–Whitehead–Segel equation [2,3] would be expected to be sufficient at least for almost straight roll patterns. However, this is true only in the limit of large Prandtl numbers. For small Prandtl numbers, curved roll patterns drive a mean flow that induces an important non-local coupling of the rolls due to the incompressibility of the fluid. It is the origin of the oscillatory and the skew-varicose instability [4]. Since the Newell–Whitehead–Segel equation does not capture the mean flow it has been extended to include an equation for a large-scale vertical vorticity mode [5].

A particularly interesting aspect of the mean flow is that it can induce persistent dynamics and disordered patterns. Thus, it has been identified as the driving force for the persistent creation and annihilation of dislocations that has

---

* Corresponding author. Tel.: +1-847-467-3345; fax: +1-847-491-2178.
E-mail address: young@statler.esam.nwu.edu (Y.-N. Young).

PII: S0167-2789(01)00389-X

been observed [6–9]. Arguably, the most interesting state that is due to the mean flow is the spiral-defect chaos observed in large-aspect ratio experiments on thin gas layers [10]. It is characterized by the appearance of various types of defects in the pattern with small rotating spirals being the ones that are visually most striking. The onset of spiral-defect chaos depends strongly on the Prandtl number, indicating that mean flows play an essential role in maintaining this state [11–14].

Motivated by the strong impact of mean flows on roll convection patterns, we consider in this paper the effect of such flows on the stability and dynamics of hexagonal patterns. Hexagonal patterns are commonly found in spatially extended non-equilibrium systems such as non-Boussinesq Rayleigh–Bénard convection (e.g. [15]), Marangoni convection (e.g. [16]), Turing structures in chemical systems [17], crystal growth (e.g. [18]), and surface waves on vertically vibrated liquid or granular layers (Faraday experiment) [19,20]. Not in all of these systems mean flows of the type discussed above arise. Clearly, they are relevant for the small Prandtl numbers in gas convection in very thin layers [10]. Interestingly, the skewed-varicose instability and a (transient) state similar to spiral-defect chaos have been observed also in vertically vibrated granular layers [21,22]. Since in convection they are a signature of the importance of mean flow, it may also be relevant in vertically vibrated fluids. We focus in this paper on patterns arising from a steady bifurcation, as is the case in convection. Immediately above onset, parametrically excited standing waves like those arising in the Faraday experiment behave in many respects like patterns that are due to a steady bifurcation (e.g. [23]). Our results may therefore, also be relevant for hexagon patterns in suitable Faraday experiments.

In the absence of mean flows the stability of hexagonal patterns has been studied in detail in the weakly nonlinear regime. Starting from three coupled Ginzburg–Landau-type equations for the amplitudes of the rolls that make up the hexagonal pattern two coupled phase equations have been derived that describe the dynamics of long-wave deformations of the hexagon patterns [24–27]. In these theoretical analyses two types of long-wave instabilities have been identified, a longitudinal and a transverse mode, with the longitudinal mode being relevant only for Rayleigh numbers very close to the saddle-node bifurcation at which the hexagons first appear. These long-wave perturbations are captured by phase equations even in the strongly nonlinear regime [27]. In a more detailed analysis also perturbations with arbitrary wavenumber and simulations of the nonlinear evolution ensuing from the instabilities have been included [28]. The instabilities typically lead to the formation of penta–hepta defects (PHDs) [29–32]. Specifically, for convection at large Prandtl numbers driven by a combination of buoyancy and surface tension the stability of hexagons and their dynamics has been investigated in [33]. Experimentally, the side-band instabilities of hexagonal convection patterns have not been studied in detail. A contributing factor has been that controlled changes in the wavenumber of the pattern are considerably more difficult to effect than in systems like Taylor-vortex flow, where detailed agreement between experiment and theory has been achieved (e.g. [34,35]). Recently, however, it has been possible to use localized heating as a printing technique for convection patterns [36,37], which allowed a detailed analysis of the stability of hexagonal patterns in Bénard–Marangoni convection [36].

In our analysis of the linear stability of hexagons coupled to a two-dimensional mean flow, we find that the mean flow couples only to one of the two long-wave modes. As a consequence, for sufficiently small Prandtl numbers each of the two long-wave instabilities dominates in a separate, experimentally accessible parameter regime. The nonlinear evolution of both instabilities leads to the formation of defects. We study their motion and briefly touch upon its impact on disordered patterns and grain boundaries.

This paper is organized as follows: first we formulate the problem extending previous work on the mean flow generated by roll convection [38,39]. We then study the stability of the hexagonal pattern with respect to side-band perturbations (Section 2). In Section 3, the nonlinear evolution of the side-band instabilities is investigated numerically, emphasizing the different evolution of the longitudinal and the transverse phase modes that destabilize the hexagons. There, we also study the transition from hexagonal to roll patterns triggered by the side-band instabilities.

In Section 4, we investigate numerically the dynamics of defects and of grain boundaries in the presence of mean flow. Section 5 gives some conclusions.

2. Formulation and stability analysis

2.1. Formulation

The interaction between weakly nonlinear convection rolls and the mean flow generated by them has been investigated for Rayleigh–Bénard convection with both no-slip and stress-free boundary conditions at the top and bottom plate [38,39]. Expanding the fluid velocity in terms of the complex amplitude A of the convection rolls and the real streamfunction Q for the two-dimensional mean flow as ($\epsilon \ll 1$)

$$\mathbf{v}(\tilde{x}, \tilde{y}, \tilde{z}, \tilde{t}) = \epsilon A(x, y, t)\, \mathrm{e}^{\mathrm{i}q_c\tilde{x}}\mathbf{v}_q(\tilde{z}) + \epsilon^2\{\vec{\tilde{\nabla}} \times (Q\hat{z}) f(\tilde{z})\} + \text{h.o.t.}, \tag{1}$$

the extended Ginzburg–Landau equation for A and Q was derived, which to leading order is given by

$$\partial_t A = (\mu + (\partial_x - \mathrm{i}\lambda\partial_y^2)^2 - |A|^2)A - \mathrm{i}s_1 A\partial_y Q + \text{h.o.t.}, \tag{2}$$

$$M(Q) = 2q_1(\partial_x - \mathrm{i}\lambda\partial_y^2)\partial_y|A|^2 + \text{h.o.t.}, \tag{3}$$

where $\lambda \equiv \epsilon/2q_\mathrm{c}$ with ϵ the supercriticality parameter and q_c the critical wavenumber. For no-slip boundary conditions $M(Q) = \nabla^2 Q$ [38], whereas $M(Q) = (q_2\nabla^2\partial_t - \nabla^4)Q$ for the stress-free case [39]. To leading order, the mean flow is driven by variations in the magnitude of the convective amplitude and couples back through the advective term $\mathrm{i}s_1 A\partial_y Q = \mathrm{i}s_1 AV_x$, where V_x is the x-component of the mean flow. At higher orders a term of the form $\mathbf{V} \cdot \nabla A$ would arise as well.

For the description of hexagonal convection patterns coupled to the mean flow the treatment has to be extended to include rolls in other directions than the x-axis. The amplitudes A_i, $i = 1, 2, 3$, correspond then to rolls with wavevector $q_\mathrm{c}\hat{n}_i$. The advection term $\mathrm{i}A\partial_y Q$ in Eq. (2) is generalized as $\mathrm{i}A_j(\hat{\tau}_j \cdot \nabla)Q$, where $\hat{\tau}_j$ is the unit vector perpendicular to $\hat{n}_j$. We complete the extension of Eqs. (2) and (3) from roll to hexagonal patterns by adding non-Boussinesq quadratic terms. The minimal set of equations describing hexagons coupled to a mean flow then reads for the no-slip case

$$\partial_t A_j = (\mu + (\hat{n}_j \cdot \nabla)^2 - |A_i|^2 - \nu(|A_{j-1}|^2 + |A_{j+1}|^2))A_j + A^*_{j-1}A^*_{j+1} - \mathrm{i}\beta A_j(\hat{\tau}_j \cdot \nabla)Q, \tag{4}$$

$$\nabla^2 Q = \sum_{i=1}^{3} 2(\hat{n}_i \cdot \nabla)(\hat{\tau}_i \cdot \nabla)|A_i|^2 \tag{5}$$

with cyclic permutation on j. Here Q has been rescaled to absorb the coefficient $q_1(\beta = s_1q_1)$. The Newell–Whitehead–Segel operator in Eq. (2) reduces to $(\hat{n}_j \cdot \nabla)^2$ in the above equations as we adopt isotropic scaling for the underlying hexagonal patterns. Such isotropic scaling can lead to degeneracies in certain growth rates like that of the zigzag instability for roll convection patterns (e.g. [40,41]). For the hexagonal patterns, this is, however, not the case.

It has to be pointed out that $Q \propto \mathcal{O}(A^2)$, which makes the mean flow contribution $\mathrm{O}(A^4)$. In a systematic derivation of (4) and (5) it therefore, represents a higher-order correction term, which in the scaling employed in (4) and (5) is reflected in β being small. Formally, the mean flow is of the same order as the lowest-order nonlinear gradient terms, which capture the wavevector dependence of the quadratic resonant term $A^*_{j-1}A^*_{j+1}$. Their influence on the stability of hexagons has been studied previously [26,42,43]. Our goal is to focus on the mean flow, which in contrast to the nonlinear gradient terms induces a *non-local* interaction. In this study, we therefore neglect the nonlinear gradient terms. We note that the coupling coefficient β of the mean flow grows with decreasing Prandtl number. Based on the calculation of the coupling coefficient in the Boussinesq case [38], we expect that for Prandtl numbers of order 1 the mean flow becomes relevant sufficiently close to threshold for hexagons to be preferred over rolls [15].

The cubic coefficient ν decreases monotonically with Prandtl number from $\nu \sim 2.0$ for $Pr = 0.5$ to $\nu \sim 1.5$ for $Pr \sim 10$ [15,44]. For the numerical results in this paper we fix $\nu = 2$.

2.2. Stability analysis

We conduct a linear stability analysis of the hexagonal pattern in the long-wave approximation following the procedures in [25]. The amplitudes are perturbed around a hexagon pattern:

$$A_j = R_0\, \mathrm{e}^{\mathrm{i}q\hat{n}_j\cdot(x,y)}(1 + r_j + \mathrm{i}\phi_j), \quad j = 1, 2, 3, \tag{6}$$

where $R_0 \equiv (1 + \sqrt{1 + 4(\mu - q^2)(1 + 2\nu)})/2(1 + 2\nu)$ is the amplitude of the stationary solution with reduced wavenumber q, and r_j and ϕ_j are the amplitude and phase perturbations, respectively. We also define u and v as in [25]

$$u = R_0^2(1 - \nu) + R_0, \qquad v = 2R_0^2(1 + 2\nu) - R_0. \tag{7}$$

Here $v = 0$ corresponds to the saddle-node bifurcation at which the hexagons come into existence ($\mu_{\mathrm{SN}} = q^2 - \frac{1}{4}(1+2\nu)$), while $u = 0$ is where hexagons become unstable to the mixed mode solution ($\mu_{\mathrm{MM}} = q^2 + (\nu + 2)/(\nu - 1)^2$). Both u and v have to be greater than zero for hexagons to be stable. Upon substituting Eq. (6) into Eqs. (4) and (5) and introducing super-slow scales, $\partial_t \to \delta^2\partial_t$ and $\nabla \to \delta\nabla$ with $|\delta| \ll 1$, we can adiabatically eliminate the perturbations in the amplitude and in the total phase $\Phi \equiv \phi_1 + \phi_2 + \phi_3$ in terms of the two translation phase modes $\phi_x \equiv -(\phi_1 + \phi_2)$ and $\phi_y \equiv (\phi_2 - \phi_3)/\sqrt{3}$. The mean-flow amplitude Q can then be expressed in terms of $\vec{\phi} = (\phi_x, \phi_y)$ as

$$Q = -\frac{3R_0^2 q}{2u}(-\hat{e}_z \cdot \hat{\nabla} \times \vec{\phi}), \tag{8}$$

and one obtains the phase equation

$$\partial_t\vec{\phi} = D_\perp\hat{\nabla}^2\vec{\phi} + (D_\parallel - D_\perp)\hat{\nabla}(\hat{\nabla}\cdot\vec{\phi}) - \frac{3q\beta R_0^2}{2u}\hat{\nabla} \times (\hat{\nabla} \times \vec{\phi}), \tag{9}$$

where $D_\parallel$ and $D_\perp$ are the longitudinal and transverse phase diffusion coefficients for the hexagons in the absence of mean flow [24,26,45].

The phase equation (9) allows a decomposition of the phase vector $\vec{\phi}$ into a longitudinal (curl-free) mode $\vec{\phi}_{\mathrm{l}}$ (satisfying $\hat{e}_z \cdot \hat{\nabla} \times \vec{\phi}_{\mathrm{l}} = 0$) with growth rate

$$\sigma_{\mathrm{l}} = \frac{\mathsf{k}^2}{2}\left[-\frac{3}{2} + \frac{q^2}{u} + \frac{4q^2}{v}\right], \tag{10}$$

and a transverse (divergence-free) mode $\vec{\phi}_t$ (satisfying $\hat{\nabla} \cdot \vec{\phi}_t = 0$) with growth rate

$$\sigma_{\mathrm{t}} = \frac{\mathsf{k}^2}{2}\left[-\frac{1}{2} + \frac{q^2}{u} - \frac{3q\beta R_0^2}{u}\right]. \tag{11}$$

As expected from Eq. (8), the mean flow affects only the transverse mode. The sign of β determines whether the mean flow destabilizes the transverse mode for positive or for negative q. We also observe that the stability boundaries are invariant under the transformation $(q, \beta) \to (-q, -\beta)$. For roll convection with no-slip boundary conditions β is always negative [38].

The stability boundaries for infinite Prandtl number [28] (no mean flow, $\beta = 0$) are reviewed in Fig. 1a. It is worth noting that the regime in which the longitudinal mode (thick solid line) is the relevant destabilizing mode is typically extremely small (below the dash-dotted line in Fig. 1a) and it is very difficult to investigate that instability experimentally. In fact, even in numerical simulations of (4) with $\beta = 0$, we found it difficult to separate the dynamics of the two modes (see also [28]).

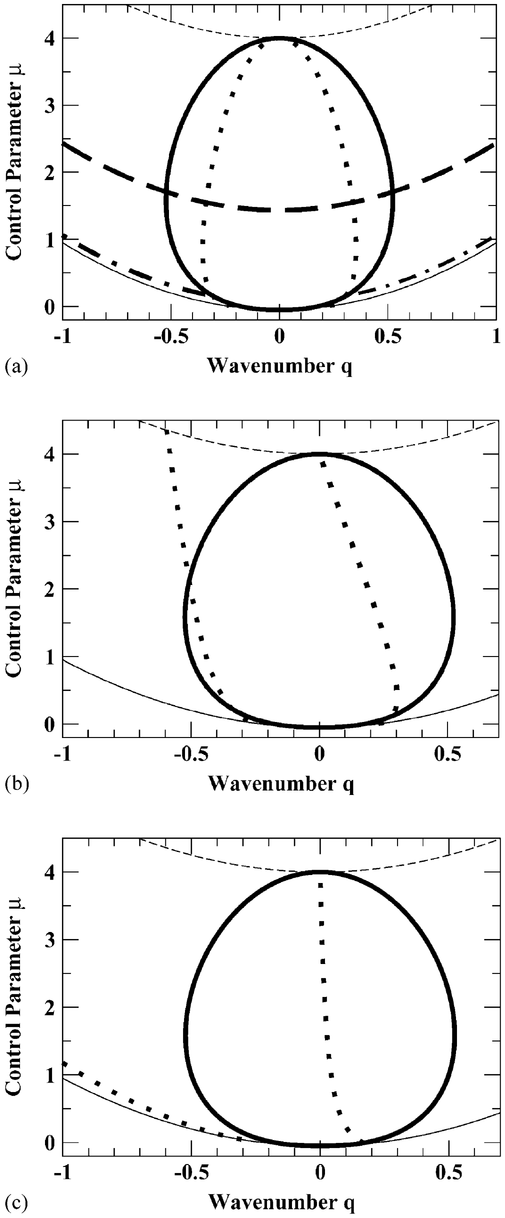

(a)

(b)

(c)

Fig. 1. Stability boundaries for infinite Prandtl number (a) and finite Prandtl numbers (b) and (c). $\beta = 0$ in (a), $\beta = -0.2$ in (b) and $\beta = -3$ in (c). Thin solid line is for the saddle-node bifurcation, thin dashed line for transition of hexagons to mixed mode solution, thick solid line for longitudinal mode, thick dotted line for transverse mode. In (a) thick dashed line for equal-energy line for hexagons and rolls, and thick dash-dotted line for cross-over from longitudinal to transverse mode. For $\beta \neq 0$ (4) and (5) are non-variational and no equal-energy line exists.

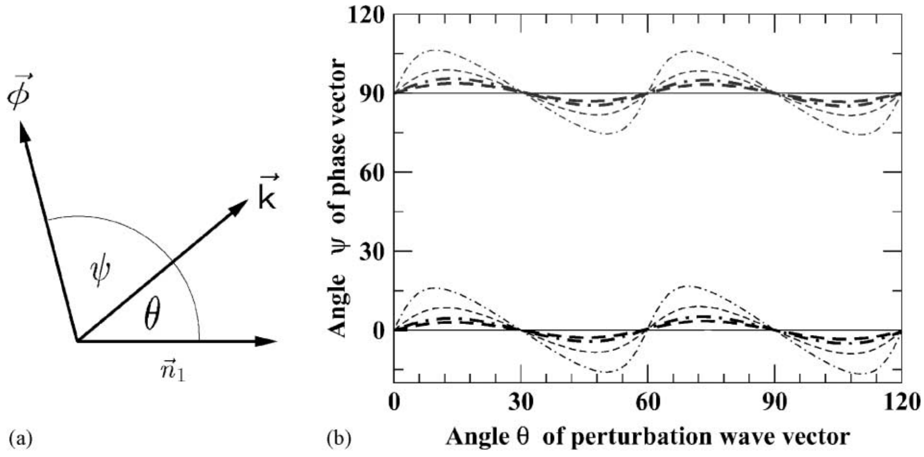

(a) (b)

Fig. 2. (a) Angles ψ and θ; (b) angle ψ (between the phase vector $\vec{\phi}$ and the perturbation wavevector $\vec{\mathsf{k}}$) as a function of the angle θ (between $\vec{\mathsf{k}}$ and $\vec{n}_1$) for $\mu = 0.5$ and $q = 0.5$. The thin lines are for coupling strength $\beta = 0$, and -0.2 for the thick lines. The solid lines are for $\mathsf{k} = 0$, the dashed lines for $\mathsf{k} = 0.192$, and the dash-dotted lines for $\mathsf{k} = 0.224$.

Fig. 1b and c shows how the stability boundaries are altered by the mean flow for $\beta = -0.2$ and -3.0, respectively. As discussed before, only the transverse mode (thick dotted line) is affected by the mean flow. It becomes destabilized for $\beta q < 0$ and stabilized for $\beta q > 0$. For larger $|\beta|$ the stabilization can be strong enough to render the longitudinal mode the only relevant destabilizing mode for $q < 0$ over the whole range of μ. Thus, for sufficiently small Prandtl numbers the two destabilizing phase modes occur on different sides of the stability balloon suggesting that a detailed comparison of the two instability modes should be possible in experiments [36]. In Section 3, we discuss the noticeably different nonlinear behavior arising from the two instabilities.

For finite perturbation wavenumbers the two phase modes are no longer purely transverse or longitudinal. Instead they can be characterized by the angle θ between the perturbation wavevector of the fastest growing modes and $\vec{n}_1$. For the 'wide-splitting' modes $\theta = n\pi/3$, whereas for the 'narrow-splitting' modes $\theta = \pi/6 + n\pi/3$ with n an integer [28]. Alternatively, the mixing between the transverse and the longitudinal modes in the phase eigenmodes[1] can be quantified by the angle ψ between the phase vector $\vec{\phi}$ and the wavevector $\vec{\mathsf{k}}$ of the perturbation eigenmode,

$$\psi \equiv \arctan\left(\frac{\hat{e}_z \cdot \hat{\nabla} \times \vec{\phi}}{\hat{\nabla} \cdot \vec{\phi}}\right), \tag{12}$$

as illustrated in Fig. 2a. For the transverse mode $\psi = \pi/2$ and for the longitudinal mode $\psi = 0$.

Fig. 2b shows the phase angle ψ for various amplitudes of $|\vec{\mathsf{k}}|$ and two values of β. We first note that the wide-splitting and narrow-splitting modes are close to the pure transverse and longitudinal modes, respectively. In fact, as the perturbation wavenumber goes to 0 the narrow-splitting mode turns into the longitudinal mode and the wide-splitting mode into the transverse phase mode. Comparing the phase angle ψ for $\beta = 0$ (thin lines) and $\beta = -0.2$ (thick lines) for the same value of the perturbation wavenumber $|\vec{\mathsf{k}}|$ indicates that the mean flow suppresses mixing between transverse and longitudinal modes.

---

[1] The mixing of the two phase modes also introduces complex eigenvalues. This occurs, however, only in parameter regimes well beyond the stability limit.

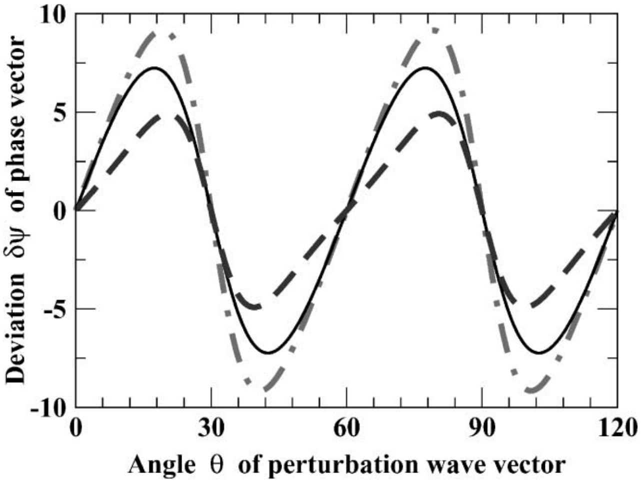

Fig. 3. The thin solid line is the fifth-order correction $\delta\psi_{\mathrm{l}} = \delta\psi_{\mathrm{t}}$ without mean flow. The thick lines give the leading-order contribution to the mean flow correction to the transverse mode ($\delta\psi_{\mathrm{t}}^1$) (thick dash-dotted line) and to the longitudinal mode ($\delta\psi_{\mathrm{l}}^1$) (thick dashed line).

To investigate the generality of the suppression of mixing due to mean flow, we go to higher order in the long-wave expansion. To obtain a systematic description to fifth order of both phase modes we need to expand around the codimension-two point at which both growth rates, σ_{t} and σ_{l}, vanish to cubic order (cf. Eqs. (10) and (11)). The derivation of the fifth-order phase equation for weak mean flow is given in Appendix A ((A.11) and (A.12)). While to third order the phase equation is still local, at fifth-order non-local terms appear. Note that in contrast to the non-local phase equation obtained in [25] the origin of the non-locality in (A.11) and (A.12) is the non-local interaction generated by the mean flow, while in [25] non-locality arose from the elimination of one of the two phase modes. As expected, the higher-order terms break the isotropy of the cubic truncation, reflecting the fact that the phase equation describes perturbations of a pattern with hexagonal symmetry. The anisotropy leads to modifications of the eigenmodes which we now discuss in terms of the phase angle ψ.

Fig. 3 shows the corrections $\delta\psi_{\mathrm{t}} \equiv \psi - \pi/2$ and $\delta\psi_{\mathrm{l}} \equiv \psi - 0$ to the phase angle ψ arising from the fourth-order derivatives and from the mean flow. In the absence of mean flow, the correction to the phase angle is the same for both phase vectors (thin solid line), indicating that the two modes remain orthogonal to each other to that order, but they are not purely transverse or longitudinal any more. The correction due to mean flow is expanded in β, $\delta\psi_{\mathrm{l,t}}^{\beta} = \beta\delta\psi_{\mathrm{l,t}}^1 + \mathcal{O}(\beta^2)$. Here we plot only the leading-order terms $\delta\psi_{\mathrm{t}}^1$ (thick dash-dotted line) and $\delta\psi_{\mathrm{l}}^1$ (thick dashed line). For $\beta < 0$ the sign of the mean flow correction, $\beta\delta\psi_{\mathrm{l,t}}^1$, is opposite to that from the fourth-order derivative without mean flow. Thus, the mean flow is seen to suppress the deviation of the modes from the transverse and longitudinal orientation, consistent with our findings for the finite wavenumber perturbations.

3. Nonlinear evolution of the side-band instabilities

We now present results from numerical simulations of Eqs. (4) and (5) using a parallel pseudo-spectral code. In Section 3, we first simulate the system for low μ to compare the nonlinear evolution of the transverse and longitudinal side-band instabilities. We then discuss the impact of the mean flow on the competition between rolls and hexagons for larger μ.

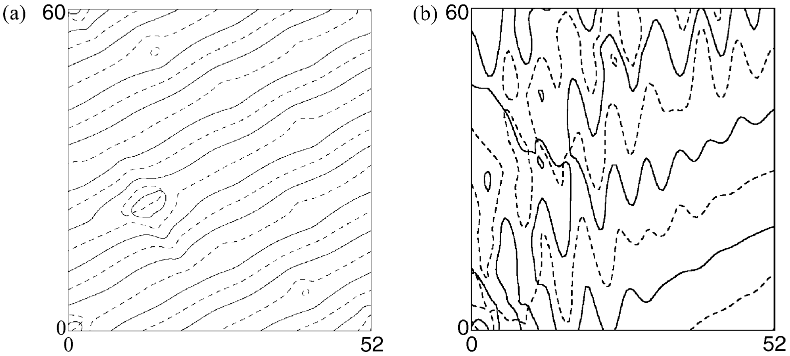

Fig. 4. Zero contour lines of the real part of the amplitude A_2 (solid lines) and of the imaginary part of A_2 (dashed): (a) only the longitudinal mode is destabilizing ($q = -0.48$); (b) only the transverse mode is destabilizing ($q = 0.17$). Only a quarter of the domain is shown.

3.1. Low μ: transverse vs. longitudinal modes

Without mean flow the nonlinear evolution of the two side-band instabilities of hexagon patterns has been studied numerically in some detail by Sushchik and Tsimring [28]. There it is found that a detailed comparison of the nonlinear evolution between wide- and narrow-splitting is extremely difficult as the range over which only the narrow-splitting (longitudinal) mode is destabilizing is very small. As discussed in Section 2.2, the mean flow couples only to the transverse/wide-splitting instability and for sufficiently small Prandtl number suppresses it completely for $\beta q > 0$. This makes it possible to compare the two instabilities in detail under comparable conditions. Figs. 4–6 show a comparison of the evolution of the two instabilities for $\mu = 0.5$, $\nu = 2$, and $\beta = -3$. The system size is $L = 104$ and the numerical resolution is 256×256. The wavenumbers of the initial, slightly perturbed regular hexagon patterns are chosen carefully to obtain the same linear growth rates for both modes. In particular, for $q = -0.48$ ($q = 0.17$) only the longitudinal (transverse) mode is destabilizing (cf. Fig. 1).

Fig. 4 shows the early evolution of the instabilities in terms of the contour lines of the real and imaginary parts of amplitude A_2. In (a) only the longitudinal mode destabilizes the pattern. It induces compressions and dilations

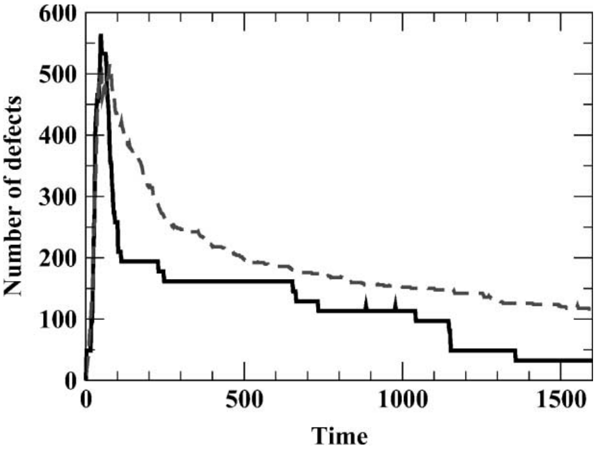

Fig. 5. Number of defects as a function of time for the longitudinal case (solid line) and transverse case (dashed line).

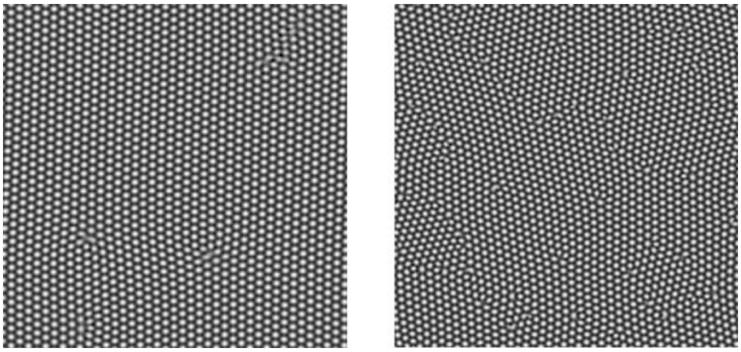

Fig. 6. Reconstructed temperature for the longitudinal mode (left panel, $q = -0.48$) and the transverse mode (right panel, $q = 0.17$) at $t = 1750$.

of the pattern. In (b) it is the transverse mode that destabilizes the pattern; it shears the amplitudes. Both lead to the formation of defects. However, the defects induced by the longitudinal mode are typically aligned along the rolls and form where the bulges are maximal.

The temporal evolution of the number of defects is shown in Fig. 5. For both modes, we define $t = 0$ when the first defect is formed. Both modes having the same growth rate it is not surprising that in both cases the defect number grows on a similar time scale. In fact, both reach roughly the same number of defects at about the same time $t \approx 50$. In both cases the subsequent ordering of the pattern appears to occur in two stages, characterized by an initial rapid annihilation of defect pairs and a later much slower phase. In the longitudinal case the defect number decreases in large steps, which are associated with the annihilation of strings of defects that are roughly aligned with the rolls, whereas no such steps are visible in the transverse case. The overall decay is substantially slower for the pattern induced by the transverse instability. This had also been found in the absence of mean flow [28].

Snapshots of the reconstructed patterns at the final time $t = 1750$ are shown in Fig. 6. Only a quarter of the whole system is shown. In the longitudinal case the defect density is already very low and the defects are essentially isolated from each other. In the transverse case, however, they are mostly part of grain boundaries that separate domains of hexagons with slightly different orientation.

To quantify the evolution of the amount of disorder in the orientation of the hexagons we determine the orientation of the local wavevector q_j relative to the roll direction $\hat{n}_j$ as defined by the angle α_j:

$$\alpha_j \equiv \arctan\left(\frac{\vec{q}_j \cdot \hat{\tau}_j}{\vec{q}_j \cdot \hat{n}_j}\right), \quad \vec{q}_j \equiv \mathrm{Re}\left(\frac{-\mathrm{i}\vec{\nabla} A_j}{A_j}\right) \quad \text{for } j = 1, 2, 3. \tag{13}$$

In Fig. 7, we plot the probability distribution function (PDF) of the orientation angle α_1 as a function of time for the cases shown in Figs. 4 and 5. Again, time $t = 0$ is where the first dislocation occurs, and we have truncated the large peaks (around $\alpha_1 = 0$) at early times so that more structures can be discerned at later times. Similar PDFs are found for the other two amplitudes, as well. For the longitudinal mode the PDF is centered around $\alpha_1 = 0$ from the beginning to the end, with the peak broadening around $t = 0$ when the first few defects appear. Thus, for all times there is only a single domain and the hexagons remain essentially aligned with their initial orientation. In the transverse case, however, the initial peak at $\alpha_1 = 0$ quickly decays and gives way to two peaks of comparable size. This occurs around the time when the maximum number of defects is reached. The bi-modal PDF indicates that the transverse mode predominantly induces domains of hexagons of two different orientations, which then co-exist for a long time. The clear separation of the two destabilizing modes in terms of the associated stability boundaries suggests that this difference in the nonlinear evolution of the instabilities should be accessible experimentally.

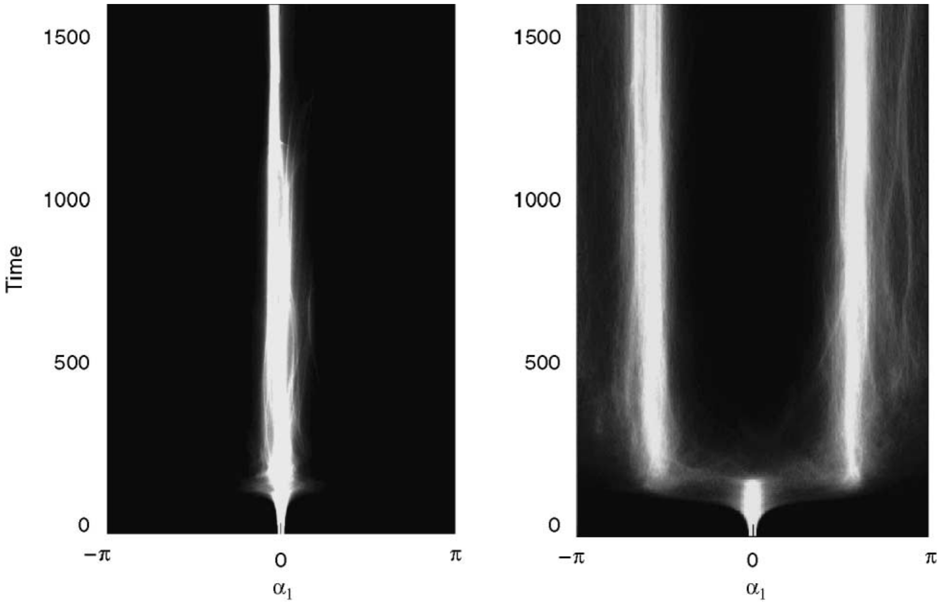

Fig. 7. Evolution of the probability distribution of α_1: the angle between $\vec{k}_1$ and $\hat{n}_1 = \hat{x}$ for the longitudinal (left) and the transverse mode (right).

3.2. High μ: hexagons vs. rolls

In the absence of mean flow, the competition between uniform hexagons and rolls is governed by the energy difference between them. For a given q, hexagons have lower energy than rolls for μ lower than a threshold value $\mu_{\mathrm{th}}(q)$ [28], while rolls are energetically favored above μ_{th}. This boundary is indicated by the dashed line in Fig. 1a. Below the dashed line, outside the stability balloon, the unstable transverse and longitudinal modes grow and evolve towards a hexagon of different wavenumbers. Above this line, rolls appear during the transients and eventually replace the hexagon.

Due to the lack of a Lyapunov functional for Eqs. (4) and (5) no simple energy arguments for the predominance of rolls or hexagons can be given and we resort to numerical simulations to locate the boundary μ_{th} between hexagons and rolls in the presence of mean flow. Table 1 lists μ_{th} for $q = \pm 0.6$ for different values of β. For example, for $\beta = -0.1$ and $q = 0.6$ we find rolls as the final state at $\mu = 1.45$ (Fig. 8, left panel), while a mixed state of rolls and hexagons is found at $\mu = 1.425$ (Fig. 8, right panel). Thus, the transition value in μ at $q = 0.6$ for $\beta = -0.1$ is between 1.425 and 1.45. The enhanced instability of the transverse mode for $q = 0.6$ leads apparently to an earlier transition to rolls when the Prandtl number is decreased. At this point it is not clear why the converse is not the case for $q = -0.6$.

Table 1
Competition between rolls and hexagons for $q = \pm 0.6$ for different β. For $\mu > \mu_{\mathrm{th}}$ side-band instabilities of hexagons lead to rolls rather than hexagons

β	μ_{th} $(q = 0.6)$	μ_{th} $(q = -0.6)$
0	1.5	1.5
−0.1	1.43	1.5
−0.2	1.35	1.5
−1.24	1.25	1.5
−3	1.1	1.5

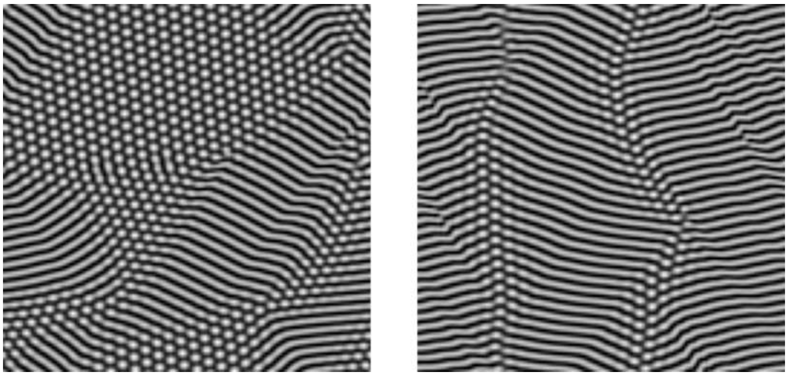

Fig. 8. Reconstructed patterns from simulating Eqs. (4) and (5) for $\beta = -0.1$ and $q = 0.6$. On the left, $\mu = 1.425$ at $t = 2000$, and $\mu = 1.45$ on the right panel at the same time.

4. Effect of mean flow on motion of defects

In this section, we study the effect of the mean flow on the motion of a PHD, which is a bound state of two dislocations in two of the three amplitudes. For large Prandtl number, where the mean flow is negligible, the far-field solution of a steadily moving PHD has been calculated [32]. We study the general case with mean flow numerically by embedding two PHDs in the system as initial conditions and measure their velocity as a function of β and q for fixed $\mu = 1$ and $\nu = 2$.

The numerical resolution is 256×256 in a system of size $L = 400$ and the time step is fixed at 0.1 for most of the results presented in this section. To satisfy the periodic boundary conditions, we place two PHDs of charges $(0, +1, -1)$ and $(0, -1, +1)$ in the computational domain, i.e. each PHD consists of two dislocations of opposite charges in the amplitudes A_2 and A_3. We also apply a circular ramp at $R = 0.4L$, beyond which the phase is set to a constant [31]. The interaction between pairs of PHD is characterized by the number $N \equiv \sum_{i=1}^{3} \delta_j^1 \delta_j^2$, where $\delta_j^{1(2)}$ is the charge of the first (second) PHD in the jth amplitude [32]. In our simulations $N = -2$ and the PHDs attract each other. Their interaction decreases with distance and we find that it becomes negligible for distances larger than 300 (for $\beta = 0$ and $q = 0$ the interaction-induced velocity is then below $v = 0.001$). Thus in the following, we place the two PHDs at least at a distance of 300 apart in the initial configuration for the velocity measurement of an individual PHD.

In the absence of mean flow, each independent PHD is found to move at a constant velocity, which vanishes at $q = 0$ [31,32]. In the presence of mean flow, we also find that isolated defects move at a constant velocity. It is shown in Fig. 9 as a function of β for $q = 0$. The range of the linear scaling with respect to the coupling strength indicates that, for small β, the contribution of the mean flow to the PHD velocity is purely additive via the advective term $\mathrm{i}\beta A(\hat{\tau} \cdot \nabla)Q$ and that the amplitudes A_i of the defect solution are only weakly affected by the mean flow. However, as $|\beta|$ increases, the defect velocity deviates significantly from the linear scaling. This is analogous to the effect of mean flow on dislocations in roll pattern [47]. Also, for larger $|\beta|$ the mean flow structure becomes distorted near the defect as shown in Fig. 10. The mean flow consists of two pairs of vortices, and is almost zero away from the defect. While for $\beta = -0.2$ (a) the two vortex pairs are of comparable strength, the pair on the right is much stronger than that on the left when β is decreased to $\beta = -1.4$ (b). This change occurs smoothly in β. When the Prandtl number is decreased further so that β is below -2 the stability limit comes very close to the background wavenumber $q = 0$ of the pattern and the PHDs trigger the formation of additional defects in their vicinity.

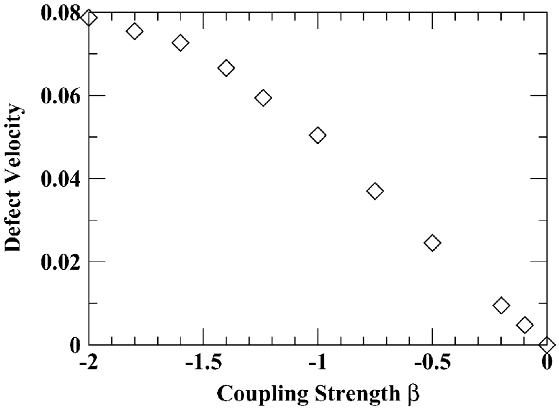

Fig. 9. Defect velocity as a function of the coupling strength β for $q = 0$ and $\mu = 1$. The defect speed scales as $\sim \beta$ for small $|\beta|$ (large Prandtl number), which in turn leads to a Prandtl number scaling $\sim Pr^{-1}$, just as in the case of rolls [46] for large Prandtl number.

The defect velocity also depends on the wavevectors $\vec{q}_i$ of the three modes making up the hexagon pattern [31]. More specifically, within Eqs. (4) and (5) it depends only on the projections $\vec{q}_i \cdot \hat{n}_i$. Fig. 11 shows the defect velocity as a function of $q \equiv \vec{q}_i \cdot \hat{n}_i$ for $\beta = 0$ (dashed line) and $\beta = -0.2$ (solid line). The mean flow shifts the defect velocity to more positive values for all q, implying that the wavenumber q_{st} at which the defect remains motionless is shifted from $q_{\mathrm{st}} = 0$ to negative values. For situations in which the evolution from disordered to more ordered patterns is dominated by defects this suggests that the wavenumber of the final state is in general not the critical wavenumber or that with the maximal growth rate but that corresponding to stationary PHDs, which depends on the Prandtl number through the mean flow.

In various simulations of the nonlinear evolution of the instabilities of the hexagon pattern, we found disordered states characterized by grain boundaries between domains of hexagons of different orientations that moved exceedingly slow. An example of such a long-lived disordered state and the associated mean flow is shown in Fig. 12a and b, where the spatial structure of such long-lived grain boundaries and the corresponding mean flow is depicted for $\mu = 1.2$, $q = 0.6$ and $\beta = -1.24$. Here the resolution is 128×128 for a system size of $L = 42$.

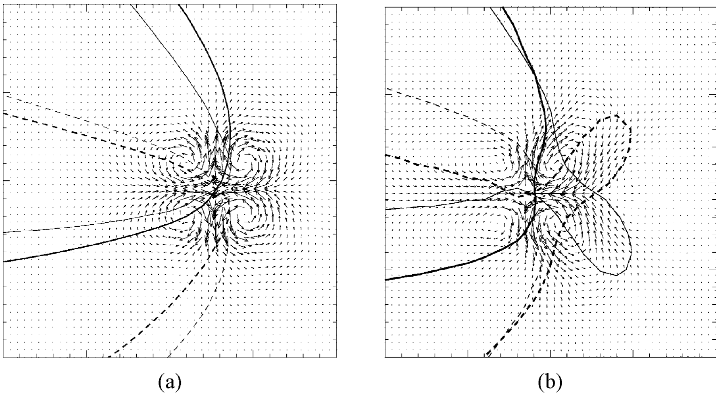
(a) (b)

Fig. 10. Mean flow structure around a PHD ($q = 0$) for: (a) $\beta = -0.2$ and (b) $\beta = -1.4$. The solid lines (dashed lines) are the zero contour lines for the real (imaginary) parts of the second amplitude.

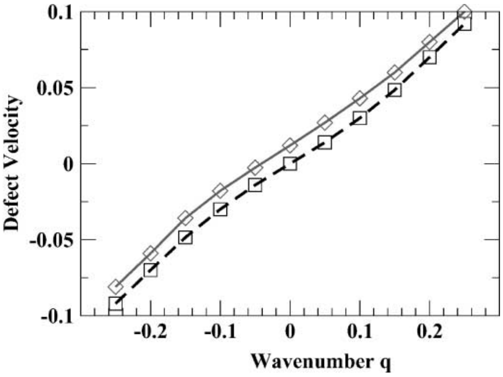

Fig. 11. Defect velocity as a function of wavenumber q for $\mu = 1$, $\beta = 0$ (dashed line) and $\beta = -0.2$ (solid line).

To identify the origin of these slow dynamics we performed simulations starting from patterns with two straight grain boundaries separating two hexagon patterns of different orientation rotated by $\pi/2$ relative to each other. For certain magnitudes of the initial wavevectors the grain boundaries did not annihilate each other but persisted for an exceedingly long time. Fig. 13a shows such an initial condition with $\vec{q}_2 = 0.2$. A contour plot of the histogram of the local wavevector of each of the three modes in the initial condition (Fig. 13a) is shown in Fig. 14a. Solid lines pertain to q_1, dashed lines to q_2, and dash-dotted lines to q_3. Despite the large magnitude of the reduced wavevector in the center domain the pattern is still linearly stable since the longitudinal component of the wavevector vanishes, $\vec{q}_j \cdot \hat{n}_j = 0$. Within (4) and (5) only this projection enters the stability conditions. Without ($\beta = 0$) and with ($\beta = -2$) mean flow the initial condition evolves to the patterns shown in Fig. 13b and c, respectively, for $t = 80\,000$ and $\mu = 0.5$. For $\beta = 0$ simulation beyond $t = 80\,000$ showed little difference in the spatial structure, and the defects seem to have reached asymptotic, immobile states at the end of the simulations. In the $\beta = -2.0$ case, although the spectra and the domain sizes remain more of less than the same after $t = 80\,000$, defects exhibit persistent lateral motion along the grain boundaries (velocity $\sim 4 \times 10^{-4}$) throughout the simulation which continues beyond $t = 160\,000$ and leads to a slightly fluctuating shape of the domains.

The histograms of the local wavevector of the final states depicted in Fig. 14b and c show that without mean flow all three wavevectors are essentially perpendicular to $\hat{n}_i$ implying that individual defects would not move.

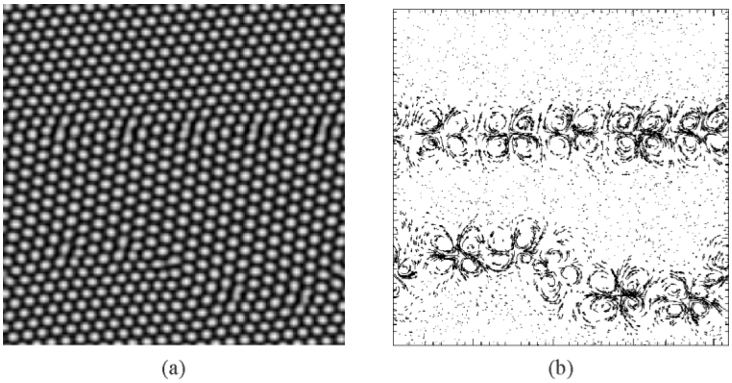
(a) (b)

Fig. 12. (a) Reconstructed hexagon pattern ($q_c = 4$) at $t \sim 14\,000$ for $\beta = -1.24$ (Prandtl number ~ 1) and $\mu = 1.2$. The initial condition was an ordered, unstable hexagon pattern with $q = 0.60$. (b) Mean flow of the state shown in (a).

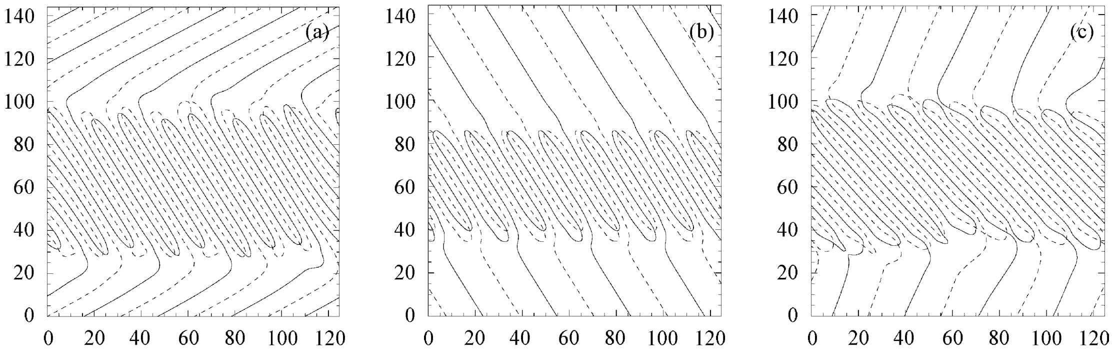

Fig. 13. Zero contour lines of the real and the imaginary part of A_2. Panel (a) is for the initial conditions, and panels (b) and (c) are snapshots at $t = 80\,000$ for $\beta = 0$ and -2.0, respectively.

In the simulation with mean flow the wavevectors are clearly not perpendicular to $\hat{n}_i$. Instead, $\vec{q}_2 \cdot \hat{n}_2 \approx -0.1$ and $\vec{q}_3 \cdot \hat{n}_3 \approx -0.1$. In separate simulations we find that for $\beta = -2$ and $\mu = 0.5$ this is the wavenumber at which individual PHDs do not move, $q_{\rm st} = -0.1$. The histogram for the third wavevector q_1, however, has peaks at $(q_x, q_y) = (-0.1, -0.05)$ and $(-0.05, 0.6)$. Thus, the two peaks have different projections onto $\hat{n}_1$ and only one of them agrees with $q_{\rm st}$. This may be related to the fact that A_1 has no dislocations in the grain boundary. In separate simulations of individual PHDs with dislocations in A_2 and A_3, we find that the velocity of the PHD depends only weakly on the wavenumber of the defect-free component (A_1), and over the whole range $-0.15 < \vec{q}_1 \cdot \hat{n}_1 < -0.05$ the PHDs are essentially motionless. Specifically, the magnitude of the velocity is below 5×10^{-4} for $\mu = 0.5$, $\beta = -2$, $\vec{q}_2 \cdot \hat{n}_2 = -0.1$, and $\vec{q}_3 \cdot \hat{n}_3 = -0.1$.

With and without mean flow, the orientation of the wavevectors in the top and bottom domains differs at the final time from that of the initial pattern, implying that in these domains the pattern rotated until the projections of their wavevectors reached $q_{\rm st}$. This suggests that, more generally, in the ordering dynamics of hexagons starting from random initial conditions the orientation of a hexagon pattern within a given domain may rotate in a similar fashion and in the long time dynamics the orientation of adjacent domains may predominantly be close to the stationarity condition for PHDs, i.e. the projections of their wavevectors onto a suitably chosen $\hat{n}$ have the same value and that value is close to $q_{\rm st}$. Of course, since our results are based on Ginzburg–Landau equations they only apply

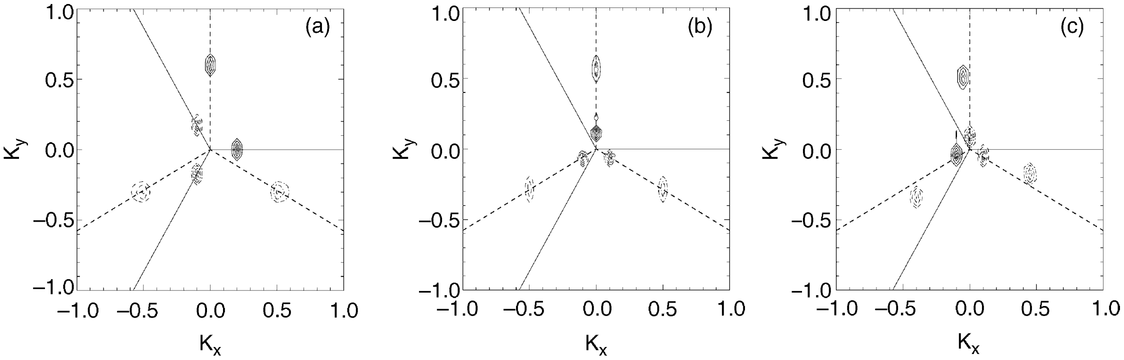

Fig. 14. Wavevector spectra of the complex amplitudes shown in Fig. 13. Panel (a) is for the initial conditions, and panels (b) and (c) are snapshots at $t = 80\,000$ for $\beta = 0$ and -2.0, respectively.

to grain boundaries across which the orientation changes only by small amounts. Furthermore, in the truncation (4) and (5) the higher-order transverse derivatives $\nabla \cdot \hat{\tau}_i$ have been neglected. They are expected to modify the stationarity condition, since the defect velocity will also depend on the transverse component of the wavevector, $\vec{q}_i \cdot \hat{\tau}_i$. The independence of the velocity on the transverse component within (4) and (5) is related to the isotropy of the system. Thus, it is expected that at higher orders the condition $\vec{q}_i \cdot \hat{n}_i = q_{\mathrm{st}}$ is replaced by a more complicated, but qualitatively similar condition suggesting similar behavior for grain boundaries.

5. Conclusion

The importance of mean flows has been noted in a wide range of pattern-forming systems. Various different types can be distinguished. In systems like binary-mixture convection [48] and in surface waves on liquids with small viscosity [49] they are driven by traveling waves. In other systems they correspond to a Goldstone mode as is the case in free-slip convection (e.g. [39,50]) or they arise from a conservation law, e.g. in systems with a deformable interface [51,52]. In this paper, we have studied the mean flow that is driven in Rayleigh–Bénard convection by deformations of the convection pattern, which becomes relevant even close to onset for fluids with low Prandtl number [5,38,39]. The most striking signatures of the mean flow in convection are the skew-varicose instability and the appearance of spiral-defect chaos. Both have been observed recently also in standing waves in vertically vibrated granular media [21,22] (the spiral-defect chaos so far only transiently). This suggests that a similar mean flow may also be relevant in that system.

Extending the usual three coupled Ginzburg–Landau equations to take the vertical vorticity mode into account [38,39], we find that the band of stable wavenumbers is always limited by one of two long-wave instabilities. In the absence of mean flow it is always the longitudinal long-wave mode that is the relevant destabilizing mode immediately above the saddle-node bifurcation at which the hexagons come first into existence, while the transverse long-wave mode is the relevant mode for larger amplitudes. The Rayleigh number for the cross-over from one to the other mode depends on the cross-coupling coefficient ν, but for realistic values it always occurs very close to the saddle-node bifurcation. The longitudinal mode is therefore, poorly accessible in the absence of mean flow (e.g. [28]). Only the transverse phase mode couples to the mean flow and we find that on the low-wavenumber side it is stabilized for sufficiently small Prandtl numbers to the extent that it is preempted by the longitudinal mode over the whole range of Rayleigh numbers from the saddle-node bifurcation to the transition to the mixed mode. As a consequence, for these Prandtl numbers the relaxation from an unstable wavenumber towards the band center is expected to be qualitatively different depending on whether the stability limits are crossed at the low- or the high-wavenumber side of the stability balloon.

Our simulations of the nonlinear evolution of the instabilities indicate that, compared to the longitudinal instability, the transverse instability leads to a considerably larger number of PHDs and to more grain boundaries separating patches of hexagons that are rotated with respect to each other. While indications of this were also found in the absence of the mean flow [28], the mean flow can make the distinction clear enough to make it worth addressing experimentally. To do so, hexagon patterns with a wavenumber away from the band center need to be initiated. Recently, it has been shown that such initial conditions can, in fact, be prepared by a suitable localized heating of the fluid [36,47]. Given the striking difference in the transients arising from the instabilities of the two modes it would be interesting to bring these techniques to bear in this system. It has to be kept in mind that the nonlinear gradient terms, which have not been kept in our calculations, may reduce the angle between the transverse and the longitudinal mode and make their distinction less pronounced.

As is the case in roll convection, the mean flow also affects the motion of defects. For the PHDs relevant in hexagonal patterns, we find that similar to the case of rolls the wavenumber at which the defect is stationary is shifted to wavenumbers smaller than the critical one. For coarsening experiments starting from random initial conditions one may therefore, expect that the eventual wavenumber of the ordered pattern may be reduced correspondingly. Our simulation suggest that the dependence of the defect velocity on the wavevector allows one to predict which grain boundaries have a particularly long life time. Furthermore, in the presence of mean flow a persistent drift of the defects in the grain boundary is observed in the simulations. One may expect that similar to the case of dislocations in roll patterns [37] the mean flow may allow two PHDs to form stable pairs if the background wavenumber is between the critical wavenumber and that corresponding to stationary defects.

Acknowledgements

We gratefully acknowledge useful discussions with G. Ahlers, E. Bodenschatz, B. Echebarria, D. Egolf and S. Venkataramani. This work is supported by NASA (NAG3-2113) and the Engineering Research Program of the Office of Basic Energy Sciences at the Department of Energy (DE-FG02-92ER14303). YY acknowledges computation support from the Argonne National Labs and the DOE-funded ASCI/FLASH Center at the University of Chicago.

Appendix A. Derivation of the nonlinear phase equations to fifth order

To facilitate the analysis we restrict ourselves to the case of weak mean flow and expand in $|\beta| \ll 1$. In the long-wave limit the codimension-two point is given by $q^{(\mathrm{ct})} = q_0 + \beta q_1$ and $R_0^{(\mathrm{ct})} = R_{00} + \beta R_{01}$ with

$$q_0 = \frac{\sqrt{2\nu+2}}{4\nu}, \qquad q_1 = \frac{3(\nu+1)}{8\nu^3}, \qquad R_{00} = \frac{1}{2\nu}, \qquad R_{01} = \frac{3\sqrt{2\nu+2}}{8\nu^3}. \tag{A.1}$$

Here we consider the magnitude R_0 as the control parameter instead of μ. To obtain explicit expressions for $(q^{(\mathrm{ct})}, R^{(\mathrm{ct})})$ we consider weak mean flow, $\beta \ll 1$ (cf. Eq. (A.1)). We rescale $X = \delta x$, $Y = \delta y$, and $T = \delta^4 t$. In this expansion δ and β are two independent small parameters. Here we expand the amplitudes $A_j = r_j\,\mathrm{e}^{\mathrm{i}q\hat{n}_j\cdot(x,y)+\mathrm{i}\phi_j}$ as

$$r_j = R_0^{(\mathrm{ct})} + \delta^2 r_{j2} + \delta^4 r_{j4} + \cdots, \tag{A.2}$$

$$\phi_j = \delta(\phi_{j0} + \delta^2\phi_{j2} + \delta^4\phi_{j4} + \cdots), \quad j = 1, 2, 3 \tag{A.3}$$

with $R_0^{(\mathrm{ct})}$ given in Eq. (A.1). The mean flow amplitude Q is expanded accordingly in δ^2

$$Q = \delta^2 Q_2 + \delta^4 Q_4 + \cdots. \tag{A.4}$$

We substitute the above expansions into Eqs. (4) and (5) and solve them at successive orders of δ. The mean flow is driven by amplitude modulations (cf. Eq. (5)) and feeds back to the phases ϕ_j via (4). Thus, at each order we first solve for the amplitudes and the mean flow in terms of the phases that were determined at the previous orders, and substitute these solutions into the phase equations to obtain the phases at the next order. At $\mathcal{O}(\delta^2)$, up to first order in β

$$r_{12} = -\frac{1}{\sqrt{2(1+\nu)}}\partial_x\phi_x - \frac{3}{8\nu(1+\nu)}(\partial_x\phi_x - 3\partial_y\phi_y)\beta, \tag{A.5}$$

$$r_{22} = -\frac{1}{4\sqrt{2(1+\nu)}}(\partial_x - \sqrt{3}\partial_y)(\phi_x - \sqrt{3}\phi_y) + \frac{3}{8\nu(1+\nu)}[(2\partial_x + \sqrt{3}\partial_y)\phi_x + \sqrt{3}\partial_x\phi_y]\beta, \tag{A.6}$$

$$r_{23} = -\frac{1}{4\sqrt{2(1+\nu)}}(\partial_x + \sqrt{3}\partial_y)(\phi_x + \sqrt{3}\phi_y) + \frac{3}{8\nu(1+\nu)}[(2\partial_x - \sqrt{3}\partial_y)\phi_x - \sqrt{3}\partial_x\phi_y]\beta, \tag{A.7}$$

$$Q_2 = -\left(\frac{3}{4\nu\sqrt{2(1+\nu)}} + \frac{9(3\nu+1)}{16\nu^3(1+\nu)}\beta\right)(-\hat{e}_z \cdot \nabla \times \vec{\phi}). \tag{A.8}$$

At cubic order we recover Eq. (9). In order to go on to fifth order we require that both σ_l and σ_t vanish (up to second order in β). As in Section 2.2, the solutions are expressed in terms of the translation modes $\phi_x = -(\phi_{20} + \phi_{30})$ and $\phi_y = (\phi_{20} - \phi_{30})/\sqrt{3}$.

Repeating the same procedures at $\mathcal{O}(\delta^4)$, we obtain r_{j4}. The expressions are too long to be displayed here. Also, at this order it is impossible to solve for Q_4 in closed form. We therefore take the Laplacian of the phase equations at this order and substitute r_{j4} and $\nabla^2 Q_4$ to obtain the nonlinear equations for ϕ_x and ϕ_y at the codimension-two point

$$\partial_t \nabla^2 \phi_x = \mathcal{L}_x + \mathrm{NL}_{x0} + \beta\,\mathrm{NL}_{x1}, \tag{A.9}$$

$$\partial_t \nabla^2 \phi_y = \mathcal{L}_y + \mathrm{NL}_{y0} + \beta\,\mathrm{NL}_{y1}, \tag{A.10}$$

where

$$\begin{aligned}\mathcal{L}_x = {} & -\frac{\nu^2}{8(\nu+1)}\nabla^2[(4\partial_x^3\partial_y + 12\partial_x\partial_y^3)\phi_y + (11\partial_x^4 + 3\partial_y^4 + 6\partial_x^2\partial_y^2)\phi_x] \\ & +\beta\frac{\sqrt{2(\nu+1)}}{16(\nu+1)^2}[(3(4+13\nu)\partial_x^5\partial_y + 6(8+3\nu)\partial_x^3\partial_y^3 + 9(4+3\nu)\partial_x\partial_y^5)\phi_y + (3(11+7\nu)\partial_x^6 \\ & +3(17+26\nu)\partial_x^4\partial_y^2 + 9(3+\nu)\partial_x^2\partial_y^4 + 9\partial_y^6)\phi_x],\end{aligned} \tag{A.11}$$

$$\begin{aligned}\mathcal{L}_y = {} & -\frac{\nu^2}{8(\nu+1)}\nabla^2[(\partial_x^4 + 9\partial_y^4 + 18\partial_x^2\partial_y^2)\phi_y + (4\partial_x^3\partial_y + 12\partial_x\partial_y^3)\phi_x] \\ & +\beta\frac{\sqrt{2(\nu+1)}}{16(\nu+1)^2}[(3\partial_x^6 + 3(19+13\nu)\partial_x^4\partial_y^2 + 9(9+2\nu)\partial_x^2\partial_y^4 + 27\partial_y^6)\phi_y + (3(4+7\nu)\partial_x^5\partial_y \\ & +3(8+13\nu)\partial_x^3\partial_y^3 + 9(4+\nu)\partial_x\partial_y^5)\phi_x].\end{aligned} \tag{A.12}$$

The nonlinear terms NL_{x0}, NL_{x1}, NL_{y0}, and NL_{y1} are too lengthy to be presented here.

References

[1] E. Bodenschatz, W. Pesch, G. Ahlers, Ann. Rev. Fluid Mech. 32 (2000) 709.
[2] A. Newell, J. Whitehead, J. Fluid Mech. 38 (1969) 279.
[3] L. Segel, J. Fluid Mech. 38 (1969) 203.
[4] F.H. Busse, Rep. Prog. Phys. 41 (1978) 1929.
[5] E. Siggia, A. Zippelius, Phys. Rev. Lett. 47 (1981) 835.
[6] A. Pocheau, V. Croquette, P. LeGal, Phys. Rev. Lett. 55 (1985) 1094.
[7] V. Croquette, P.L. Gal, A. Pocheau, R. Guglielmetti, Europhys. Lett. 1 (1986) 393.
[8] H.S. Greenside, M.C. Cross, W.M. Coughran, Phys. Rev. Lett. 60 (1988) 2269.
[9] F. Daviaud, A. Pocheau, Europhys. Lett. 9 (1989) 675.
[10] S. Morris, E. Bodenschatz, D. Cannell, G. Ahlers, Phys. Rev. Lett. 71 (1993) 2026.
[11] H. Xi, J. Gunton, J. Vinals, Phys. Rev. Lett. 71 (1993) 2030.
[12] M. Bestehorn, M. Fantz, R. Friedrich, H. Haken, Phys. Lett. A 174 (1993) 48.
[13] W. Decker, W. Pesch, A. Weber, Phys. Rev. Lett. 73 (1994) 648.
[14] J. Liu, G. Ahlers, Phys. Rev. Lett. 77 (1996) 3126.
[15] E. Bodenschatz, J.R. de Bruyn, G. Ahlers, D. Cannell, Phys. Rev. Lett. 67 (1991) 3078.
[16] M. Schatz, et al., Phys. Rev. Lett. 75 (1995) 1938.
[17] Q. Ouyang, H. Swinney, Nature 352 (1991) 610.

[18] B. Caroli, C. Caroli, B. Roulet, J. Cryst. Growth 68 (1987) 677.
[19] W. Edwards, S. Fauve, J. Fluid Mech. 278 (1994) 123.
[20] F. Melo, P. Umbanhowar, H. Swinney, Phys. Rev. Lett. 75 (1995) 3838.
[21] J.R. de Bruyn, et al., Phys. Rev. Lett. 81 (1998) 1421.
[22] J.R. de Bruyn, B.C. Lewis, M.D. Shattuck, H.L. Swinney, Phys. Rev. E 6304 (2001) 1305.
[23] H. Riecke, Europhys. Lett. 11 (1990) 213.
[24] J. Lauzeral, S. Metens, D. Walgraef, Europhys. Lett. 24 (1993) 707.
[25] R. Hoyle, Appl. Math. Lett. 8 (1995) 81.
[26] B. Echebarria, C. Pérez-García, Europhys. Lett. 43 (1998) 35.
[27] R. Hoyle, Phys. Rev. E 61 (2000) 2506.
[28] M. Sushchik, L. Tsimring, Physica D 74 (1994) 90.
[29] L. Pismen, A. Nepomnyashchy, Europhys. Lett. 24 (1993) 461.
[30] M. Rabinovich, L. Tsimring, Phys. Rev. E 49 (1994) 35.
[31] L. Tsimring, Phys. Rev. Lett. 74 (1995) 4201.
[32] L. Tsimring, Physica D 89 (1996) 368.
[33] M. Bestehorn, Phys. Rev. E 48 (1993) 3622.
[34] M. Dominguez-Lerma, D. Cannell, G. Ahlers, Phys. Rev. A 34 (1986) 4956.
[35] H. Riecke, H.-G. Paap, Phys. Rev. A 33 (1986) 547.
[36] D. Semwogerere, M.F. Schatz, Phys. Rev. Lett., submitted for publication.
[37] E. Bodenschatz, Private communication.
[38] W. Decker, W. Pesch, J. Phys. II (Paris) 4 (1994) 419.
[39] A. Bernoff, Eur. J. Appl. Math. 5 (1994) 267.
[40] T. Callahan, E. Knobloch, Phys. Rev. E 64 (2001) 6214.
[41] B. Echebarria, H. Riecke, Physica D 158 (2001) 45.
[42] J. Bragard, M.G. Velarde, J. Fluid Mech. 368 (1998) 165.
[43] A. Nuz, et al., Physica D 135 (2000) 233.
[44] F.H. Busse, J. Fluid Mech. 30 (1967) 625.
[45] B. Echebarria, H. Riecke, Physica D 139 (2000) 97.
[46] J.A. Whitehead, J. Fluid Mech. 75 (1976) 715.
[47] E. Bodenschatz, W. Pesch, Private communication.
[48] T. Clune, E. Knobloch, Physica D 61 (1992) 106.
[49] J.M. Vega, E. Knobloch, C. Martel, Physica D 154 (2001) 313.
[50] P.C. Matthews, S.M. Cox, Phys. Rev. E 62 (2000) 1473.
[51] A. Golovin, A. Nepomnyashchy, L. Pismen, Physica D 81 (1995) 117.
[52] M. Renardy, Y. Renardy, Phys. Fluids 5 (1993) 2738.